iScience

CellPress
OPEN ACCESS

Article

Accelerating ammonia synthesis in a membraneless flow electrolyzer through coupling ambient dinitrogen oxidation and water splitting

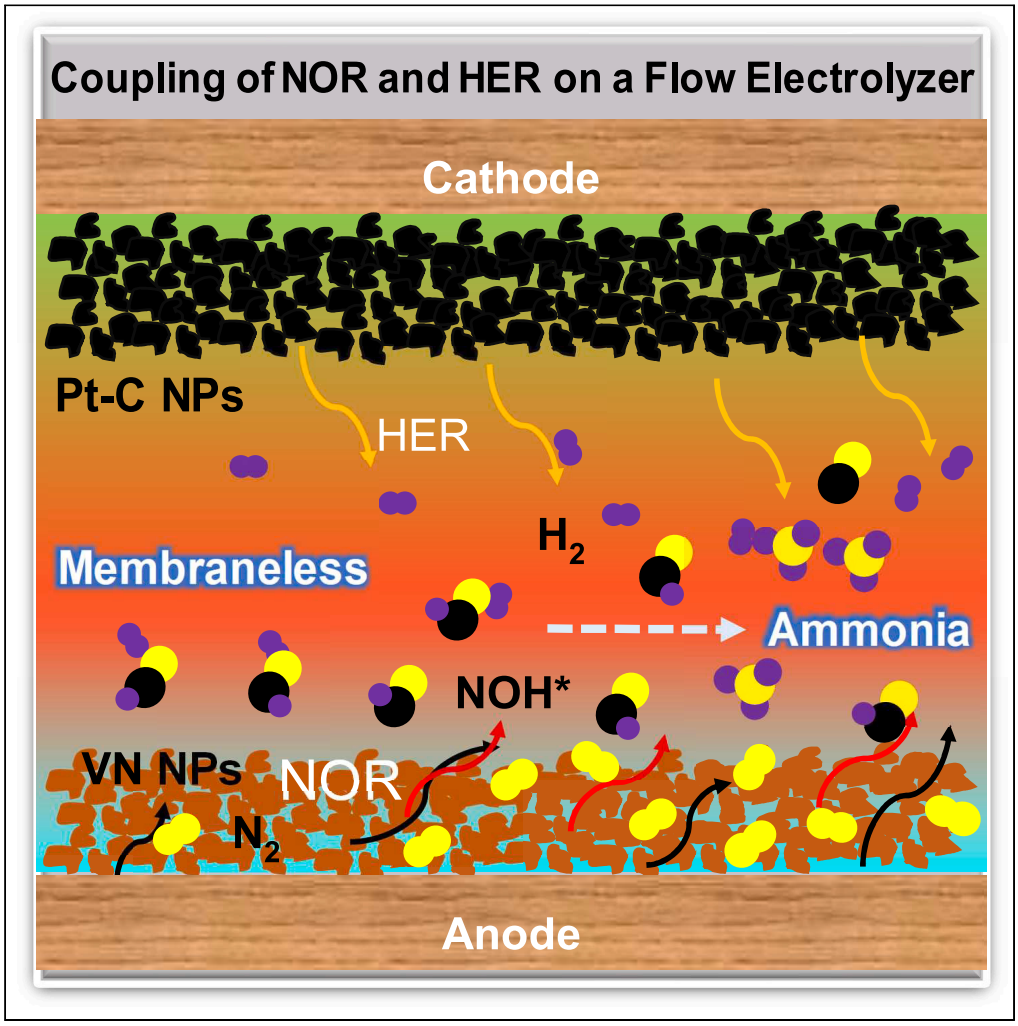

Jing-Jing Lv, Zhe Li, Jiaju Fu, Wenlei Zhu

fujiaju@iccas.ac.cn (J.F.)
wenleizhu@nju.edu.cn (W.Z.)

Highlights

The NOR and HER were coupled in a designed membraneless flow electrolyzer

The ammonia was formed on the surface of VN nanoparticles at an oxidation potential

The proposed method alleviated ammonia contamination and promoted ammonia production

The coupling strategy showed good universality for the other type of VN microparticles

Lv et al., iScience *26*, 106407
April 21, 2023
https://doi.org/10.1016/j.isci.2023.106407

iScience

CellPress
OPEN ACCESS

Article

Accelerating ammonia synthesis in a membraneless flow electrolyzer through coupling ambient dinitrogen oxidation and water splitting

Jing-Jing Lv,[2,3] Zhe Li,[1,3] Jiaju Fu,[1,*] and Wenlei Zhu[1,4,*]

SUMMARY

An electrochemical approach for ammonia production is successfully developed by coupling the anodic dinitrogen oxidation reaction (NOR) and cathodic hydrogen evolution reaction (HER) within a well-designed membraneless flow electrolyzer. The obtained reactor shows the preferential yield of ammonia over nitrogen oxides on the vanadium nitride catalyst surface. At an applied oxidation potential of 2.25 V versus the reversible hydrogen electrode (vs RHE), a promoted ammonia production rate and Faradaic efficiency (FE) were obtained with 9.9 mmol g^{-1} h^{-1} (0.029 mmol cm^{-2} h^{-1}) and 4.8%, respectively. Besides, the negative affection of ammonia contamination is efficiently alleviated. Density functional theory calculations revealed that the thermodynamic energy needed to produce ammonia (−0.63 eV) is far lower than that of producing nitrogen oxide (0.96 eV) from hydrogenated nitrogen oxides [*N_2OH] splitting, confirming the coupling of NOR and HER.

INTRODUCTION

The cyclic transformation of nitrogen is one of the vital material cycles in the biosphere.[1–3] The fixing dinitrogen from the atmosphere occupies a pivotal role and has been industrially realized to synthesize ammonia by the Haber−Bosch (H−B) process since the early 1900s.[4,5] This technological innovation has unburdened mankind from solely relying on biological-based nitrogen fixation and revolutionized the agricultural production system.[1,3] However, the energy sources and the hydrogen used in the H–B process still primarily originated from fossil fuel combustion and methane reforming. All of which released tremendous amounts of greenhouse gases and excessive energy consumption.[6,7] Therefore, the development of advanced energy-conservation nitrogen fixation methods with less greenhouse gas emissions is urgently needed.

Coupling renewable energy and a water-based hydrogen source,[8–11] the electrochemical fixation of dinitrogen (EFN) under ambient conditions was on the rise in recent years.[1,7,12] To date, most of the EFN research focused on the dinitrogen reduction reaction (NRR) to form ammonia (Figure 1), including novel electrocatalysts, reaction optimization, and exploring electrocatalytic mechanisms.[13–20] Unfortunately, considering the inert molecular structure of N_2 (bond energy: 940.95 kJ mol^{-1}) and ubiquitous ammonia in aqueous solutions, organic solvents, catalysts, membranes, etc., satisfactory results on NRR from H_2O and N_2 under ambient conditions are significantly limited.[21–25] To date, the EFN process is still far from ideal. The intractable challenges remain in low efficiency, poor conversion, severe contamination, unsound mechanism, etc.[22,25] Therefore, the need of superior and efficient protocols to enhance ENF performance is critical to overcome ammonia contamination. On top of that, the probing mechanism is also necessary to investigate.

Heuristically, the fixation of nitrogen could be realized by forming nitrogen oxides (NO_x) from the oxidation of N_2 activated by lightning,[1,26] plasma,[27] as well as other mimetic process in electrocatalytic nitrogen oxidation reaction (NOR, Figure 1).[28,29] Meanwhile, significant progress has been achieved in converting NO_x into ammonia by electrocatalytic hydrogenation with high-efficiency catalysts (Figure 1).[30–33] In addition, the microflow cell configuration could substantially improve the electrocatalytic performance of various reduction reactions in both aqueous[34–38] and organic electrolytes.[8] Given that the Nafion membrane used in NRR systems has been experimentally confirmed with unfavorable outcome such as

[1]School of Chemistry and Chemical Engineering, School of Environment, State Key Laboratory of Analytical Chemistry for Life Science, State Key Laboratory of Pollution Control and Resource Reuse, Nanjing University, Nanjing 210023, China

[2]Wenzhou Key Lab of Advanced Energy Storage and Conversion, Zhejiang Province Key Lab of Leather Engineering, College of Chemistry and Materials Engineering, Wenzhou University, Wenzhou 325035, China

[3]These authors contributed equally

[4]Lead contact

*Correspondence: fujiaju@iccas.ac.cn (J.F.), wenleizhu@nju.edu.cn (W.Z.)

https://doi.org/10.1016/j.isci.2023.106407

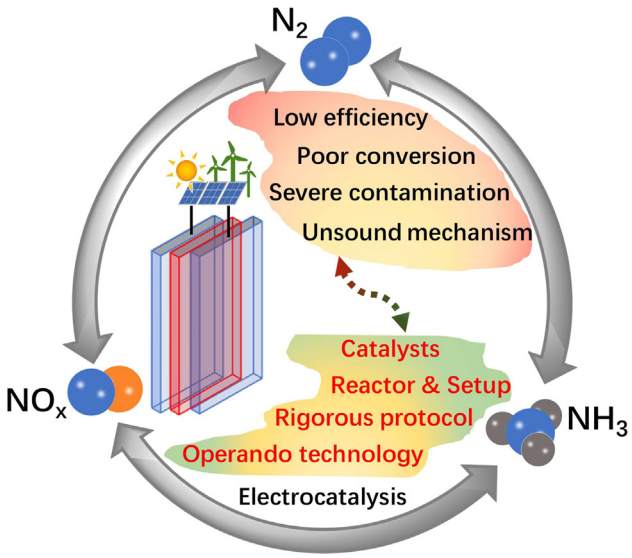

Figure 1. Schematic of electrocatalytic nitrogen fixation and potential challenges

imprecise ammonia quantification and long-term instability in practical scenarios[23,39] by accumulating and releasing ammonium ions (NH_4^+) during ion exchange with acid groups,[22,39,40] therefore, it is logical to establish a membraneless microflow cell system with an integrated protocol of NOR and NO_x reduction reaction to achieve the aforementioned synergistic EFN process.

In this work, we proposed a novel pathway for ambient ammonia synthesis that successfully couples the electrochemical NOR with the hydrogen evolution reaction (HER) process (ENH) in a single microflow cell unit (Figure 2). Commercial vanadium nitride nanoparticles (VN NPs) were applied as the electrocatalyst to *in-situ* oxidize N_2 into $*NO_x$ species at the anode side, while the H_2 from cathodic water splitting was then transferred to the anode and subsequently reduced the $*NO_x$ species into ammonia. The coupled anodic and cathodic reactions in one single flow electrolyzer effectively alleviated circumambient ammonia contamination and promoted ammonia production (ammonia yield rate: 9.9 mmol g^{-1} h^{-1} (0.029 mmol cm^{-2} h^{-1}) and FE: 4.8%). Furthermore, density functional theory (DFT) calculations indicate that the thermodynamic energy barrier to produce ammonia is much smaller than that of nitrogen oxide, confirming a preferential coupling process for ammonia synthesis, by providing a novel way for the hydrogenation process in the formation of ammonia during the electrochemical fixation of nitrogen. We believe the proposed strategy could create new insights into promoting ammonia synthesis under ambient conditions.

RESULTS

Owing to the preferential N_2 adsorption energy,[9,41,42] the active interface properties, and the strong oxidizing tendency,[43] the commercial VN NPs were loaded on a gas diffusion layer (GDL) and conducted

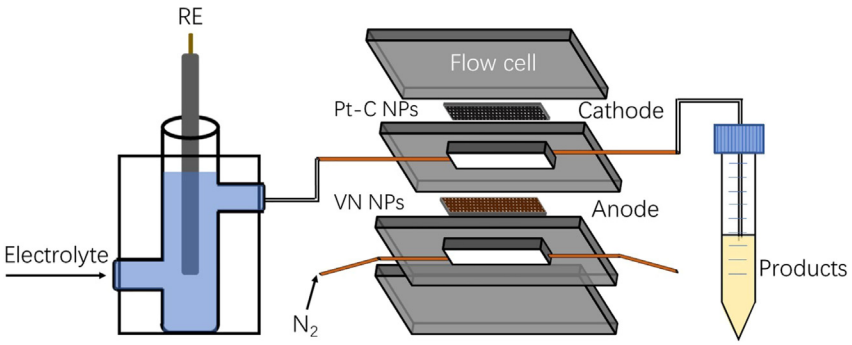

Figure 2. Schematic representation of the electrochemical flow cell used in this work

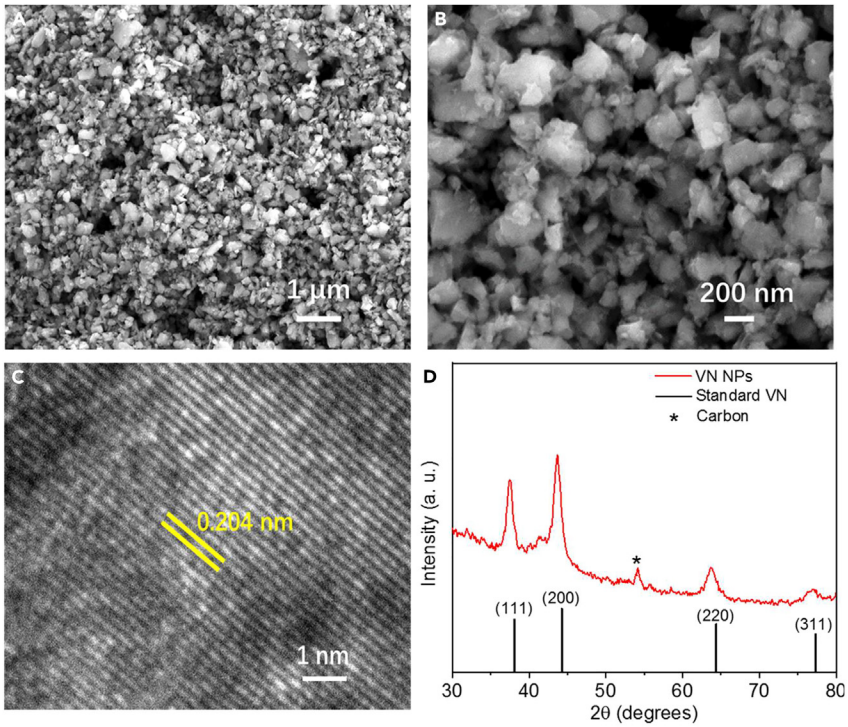

Figure 3. Microstructural characterizations of VN NPs
(A) SEM image, (B) SEM image, (C) HRTEM image, and (D) PXRD spectrum.

as the anodic catalyst in this work (see STAR Methods for details). Scanning electron microscopy (SEM) images (Figures 3A and 3B) showed the well-dispersed nature of the ca. 200-nm-diameter nanoparticles on the GDL and good porosity of the catalyst layer, both of which are favorable for stabilizing the electrode−electrolyte interface in the flow cell system.[44] The corresponding high-resolution transmission electron microscopy (HRTEM) image illustrates well-resolved lattice fringes with an interplanar distance of 0.204 nm, this can be indexed to the (200) plane of *fcc* phased VN crystal (Figure 3C). In addition, the powder X-ray diffraction (PXRD) pattern (Figure 3D) of the VN nanoparticles further confirmed the face-centered cubic crystal structure of the as-purchased VN NPs (JCPDS No. 25-1252).[9] Surface composition analysis of the as-obtained electrode was accomplished by X-ray photoelectron spectroscopy (XPS, Figure S1A) and energy-dispersive X-ray spectroscopy (EDS, Figure S1B), indicating the presence of V, N, C, and O. These characterizations jointly confirmed that the commercial VN NPs can be an ideal candidate for catalyzing ENH process in the flow cell.

The ENH performance of the as-prepared electrodes was systematically assessed in a membraneless flow cell electrolyzer with two compartments (Figures 2 and 4A), in which the anodic reaction (NOR) and cathodic reaction (HER) were coupled to facilitate the production of ammonia (see STAR Methods for details). The amount of produced ammonia was quantified via a combination of the Nessler method and ^{1}H NMR spectroscopy (see STAR Methods for details) and the corresponding calibration curves for the NH_4^+ assay are presented in Figure S2. We first optimized the ENH performance of the electrolyzer by screening different catalyst loadings (Table S1), types of electrolytes (Table S2), flow rates of electrolytes (Table S3), and current densities (Figures 4B and 4C, Table S4). With a catalyst loading of 3 mg cm^{-2}, electrolyte of 0.05 M H_2SO_4, and current density of 50 mA cm^{-2}, the optimal ammonia yield rate and FE on the as-described membraneless flow cell electrolyzer were obtained with 9.90 mmol g^{-1} h^{-1} (0.029 mmol cm^{-2} h^{-1}) and 4.8%, respectively, at a potential of 2.25 V vs RHE. At a higher current density (100 mA cm^{-2}), the cell yielded a highly unstable current profile and lower ENH activity likely resulted from the gas accumulation and severe corrosion of the carbon substrate at the anode (Figures 4B and 4C).[34,45] It is worth mentioning that the optimized flow rate of electrolyte was finally chosen as 1 mL min^{-1}, which can be attributed to the severely poor stability and insufficient yield rate of ammonia at higher flow rates (2 and

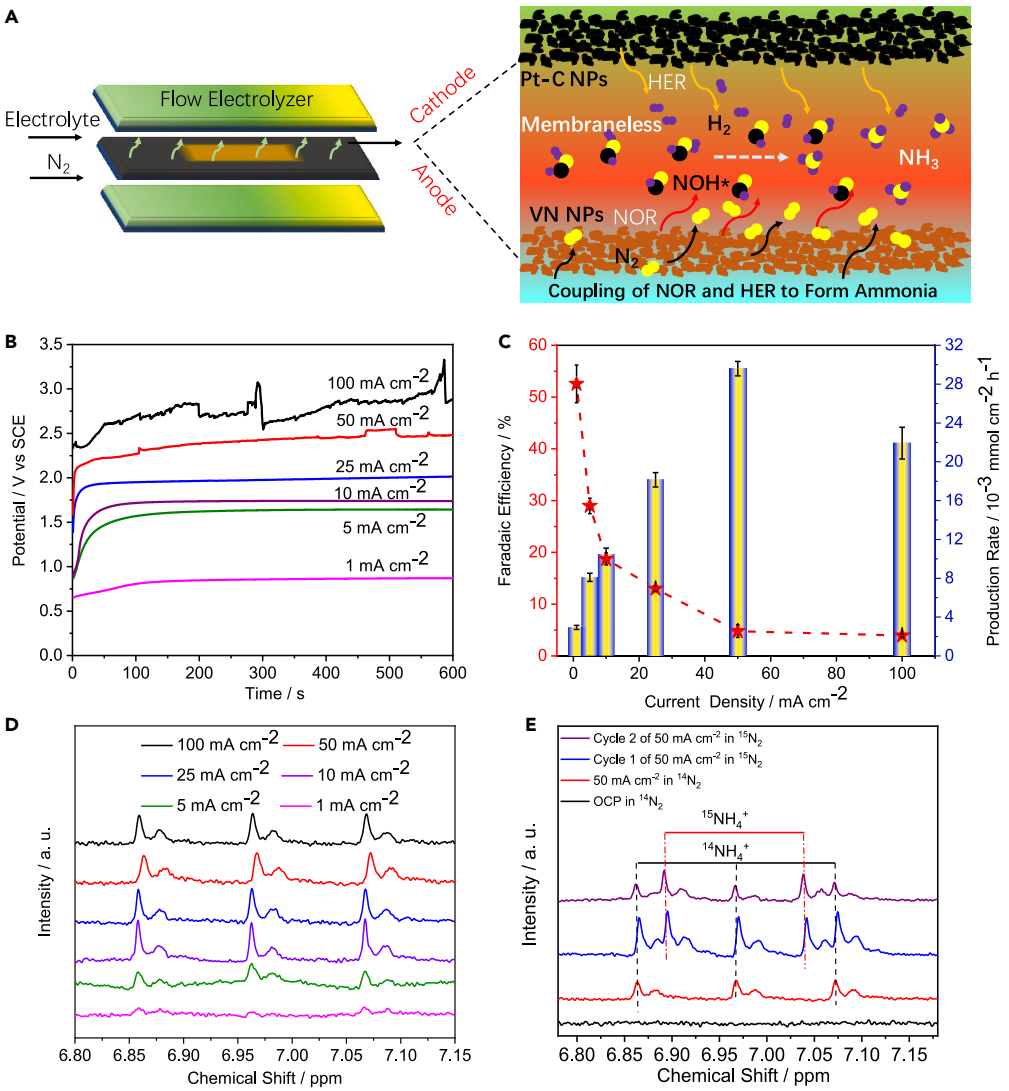

Figure 4. The electrochemical performance of the VN NPs electrode

(A) Schematic of nitrogen fixation by the membraneless flow electrolyzer.

(B) Chronopotentiometric curves for ENH at various current densities in 0.05 M H_2SO_4 electrolyte.

(C) FEs and yield rates of ammonia under different current densities. The error bars represent the s.d. for at least three independent measurements.

(D) ^{1}H NMR spectra for the collected samples.

(E) ^{1}H NMR spectra for the obtained electrolytes from different operating parameters.

5 mL min^{-1}, Table S3). The production of ammonia from ENH was further analyzed according to the ^{1}H NMR results at different current densities (Figures 4D and 5A). In addition, the $^{15}N_2$ and $^{14}N_2$ isotope labeling results (Figure 4E) within 5 min for the first or second cycle clarify that the nitrogen source is from N_2 activation (see STAR Methods for details), excluding N leaching from VN or N concentration from surrounding contamination.

A comparison of the ENH performance in this work and reported literature is shown in Table 1. In terms of the current density, ammonia yield rate, FE, and energy efficiency, the electrocatalytic performance in this work is superior to the reported literature.[8,9,13,16–18,28,29,46,47] By replacing feed gas, the steady-state linear sweep voltammogram (LSV) curves for the VN NPs (Figure 5B) showed a decline in current density with the sequence of N_2, air, and Ar-saturated electrolyte. The enhanced current in N_2 and air-saturated electrolytes

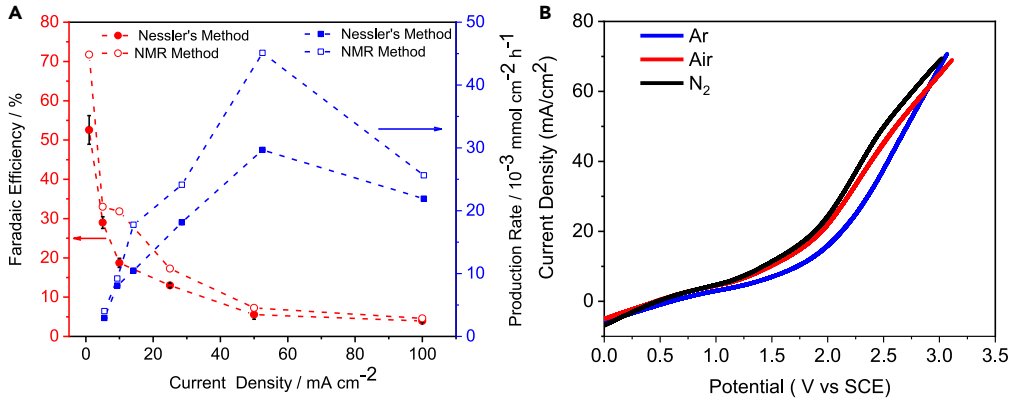

Figure 5. Quantification and verification of produced ammonia from ENH

(A) Comparison of Nessler method and NMR method for quantifying the NH_4^+ obtained from different current densities. The error bars represent the s.d. for at least three independent measurements.

(B) LSV curves of VN NPs in N_2-saturated, air-saturated, and Ar-saturated 0.05 M H_2SO_4 electrolyte.

should result from the ENH process.[48] The trace yield of ammonia from the Ar-saturated electrolyte is likely contributed from the NO_x^- residues in the electrolyte or catalyst.[24] The corresponding higher ENH performance in N_2 and air-saturated electrolytes confirms that the catalytic conversion of N_2 to ammonia occurs in this system (Table S5). Furthermore, significant amounts of ammonia were also produced on bulk VN (Figure S3 and S4), suggesting that the formation of ammonia is universal in VN-catalyzed ENH.

As shown in Figures 6A and 7 inset, the obtained VN NPs have a negligible decay in ammonia yield and FE during five rounds of recycling test at 50 mA cm^{-2}, indicating their decent stability for ENH. The applied potential positively shifted with additional cycles (Figure 7), which could also mainly originate from the carbon corrosion of the GDL substrate.[45] After the stability test, photographs of the VN NPs-deposited GDL show that the VN NPs remained in good condition on the front side, while severe etching occurred on the back side (Figure S5). In addition, the GC spectrum reveals the formation of monoxide (Figure S6) during the ENH process, further verifying the existence of the side reaction of carbon oxidation.

Furthermore, when the applied current density was decreased to 10 mA cm^{-2}, the ENH process achieved stable potential curves (Figure S7A) and kept constant for twelve cycles (Figure S7B), indicating that carbon erosion could cause negative effects on the ENH process. This further suggested the necessity to explore suitable carbon-free gas diffusion layers in future studies. More importantly, the basic physical structures of

Table 1. Comparison of the catalytic performances (j-Current density, Faradaic efficiency-FE, Ammonia yield rate, and Energy efficiency-EE) of VN NPs toward ENH with recently reported NRR and NOR catalysts at ambient conditions

Electrocatalyst	*j* (mA cm^{-2})	FE (%)	Ammonia yield rate (mmol g^{-1} h^{-1})	Ammonia yield rate (mmol cm^{-2} h^{-1})	EE (kJ mol^{-1} NH_3)	Reference
VN NPs	50	4.78	9.9	$3.0*10^{-2}$	15542	This work
VN nanoparticles	0.096	6	2.4	$1.2*10^{-3}$	–	Yang et al.[9]
BiNCs/CB/CP	4.2	66	200	$5.2*10^{-2}$	264	Hao et al.[13]
Cu/PI-300	1.7	6.56	0.2	$1.01*10^{-3}$	–	Lin et al.[46]
Au-TiO_2/CP	$1.6*10^{-3}$	8.1	1.3	$1.9*10^{-5}$	715	Shi et al.[47]
Fe/FTO	$1.4*10^{-3}$	60	0.12	$1.7*10^{-5}$	386	Zhou et al.[16]
Au film	$1.1*10^{-3}$	0.12	–	$1.4*10^{-5}$	120606	Yao et al.[18]
PEBCD/CC	$2.8*10^{-3}$	2.85	0.027	$3.4*10^{-5}$	5078	Chen et al.[17]
Stainless steel cloth, GDE	8.8	35.3	–	$1.1*10^{-1}$	–	Lazouski et al.[8]
$ZnFe_xCo_{2-x}O_4$ spinel oxides	0.01	10.1	0.13 (NO_3^-)	$3.3*10^{-5}$	–	Dai et al.[28]
Ru/TiO_2	3.0	26.1	0.16 (NO_3^-)	$1.6*10^{-5}$	–	Kuang et al.[29]

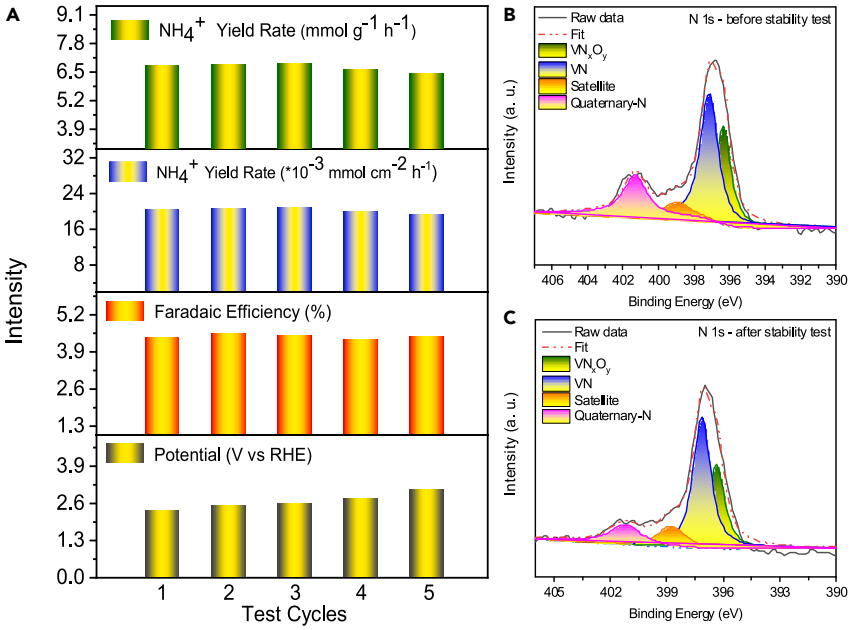

Figure 6. Electrochemical stability investigation

(A) Five cycle ENH performance of VN NPs at 50 mA cm^{-2}.

(B) High-resolution N1s XPS spectra of VN NPs before the ENH stability test.

(C) High-resolution N1s XPS spectra of VN NPs after the ENH stability test.

the VN NPs observed on SEM (Figure S8A), HRTEM (Figure S8B), PXRD (Figure S9A), XPS (Figures S9B, S9C, and S10A), and EDS (Figure S10B) were all well maintained after the stability test at 50 mA cm^{-2}, further confirming the excellent durability of the ENH system. For instance, the nitrogen atomic content is almost unchanged as comparing the VN NPs before (11.04 at%) and after (10.94 at%) stability test at 50 mA cm^{-2} (Figures S1A and S10A). As illustrated from the N1s XPS spectra of VN NPs before and after the ENH stability test (Figures 6B and 6C), the obvious higher N-containing species on VN NPs before the stability test should be originated from quaternary-N of ammonia, which could be due to the adherence of atmospheric

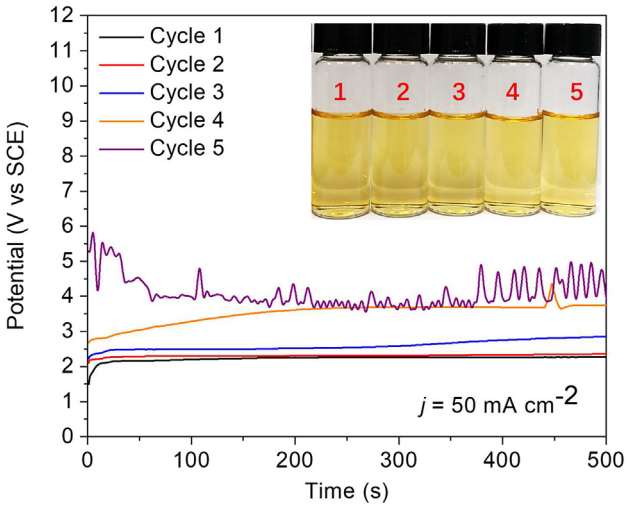

Figure 7. Electrochemical stability investigation

Five cycle chronopotentiometric curves of ENH process by using VN NPs as the catalyst in 0.05 M H_2SO_4 (inset: the corresponding H_2SO_4 electrolyte solution reacted with the Nessler agent).

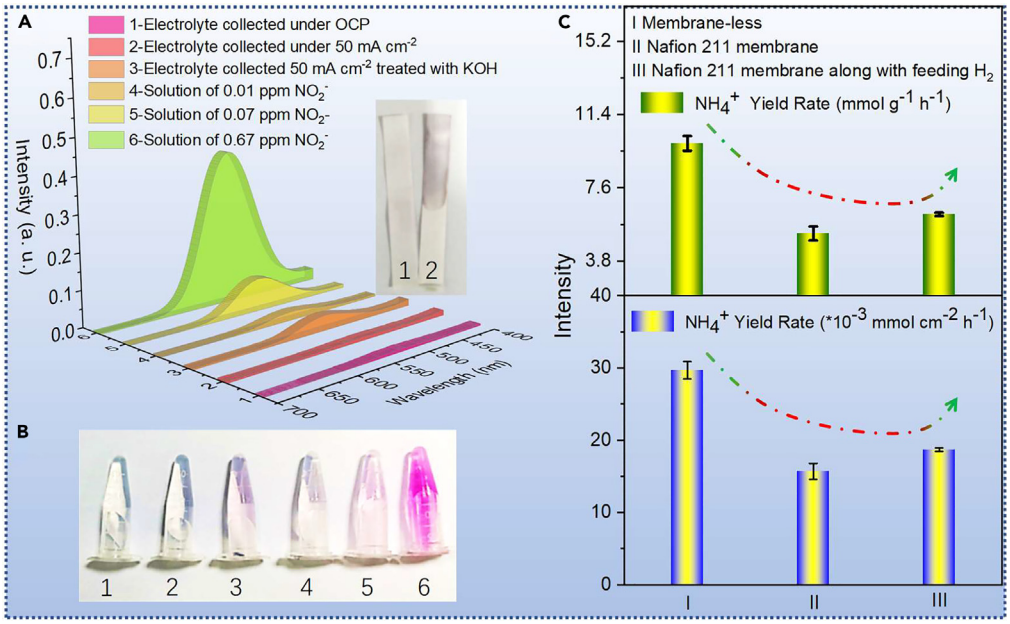

Figure 8. Control experiments for mechanism investigation

(A) UV spectra. The inset in a, shows KI test paper treated with the corresponding samples.

(B) Photographs of different samples after Azide reaction.

(C) Comparison of ammonia yield rates obtained with the membraneless, membrane, and H_2 feed membrane flow electrolyzer at 50 mA cm^{-2}. The error bars represent the s.d. for at least three independent measurements.

ammonia contaminant on the commercial VN NPs as stored in the ambient condition.[49] The other nitrogen species show almost no change, such as VN and VN_xO_y.[9,50] These results support the conclusion that the produced ammonia is derived from ENH.

Systematic control experiments were conducted to investigate the reaction mechanism of the coupled NOR and HER process. As shown in Figures 8A and 8B, in the instantly collected solution, the trace amount of NO_2 was converted into NO_2^- by reacting with KOH, triggering a chromogenic azide reaction (Table 2), and turning the solution into a magenta color with an UV-visible absorption peak ca. 550 nm.[51] Meanwhile, with the I_2 formed from the reaction of NO_2 and potassium iodide (KI), KI test paper displayed a blue color when dipped in the outlet solution from the ENH reaction (Figure 8A inset, Table 2).[52] The chromogenic reaction of NO_2 evidenced the occurrence of the NOR at the anode, suggesting the smooth proceeding electrooxidation process to the *in-situ*-form $*NO_x$ intermediates. Moreover, to determine the quantity of NO_2^- contamination in N_2 source, the experiment of simple N_2 purging under open circuit potential (OCP) for about 10 min was performed. As shown in the Figures S11A and S11B, the collected electrolyte has no color reaction with KI tester and cannot trigger a chromogenic azide reaction, indicating the trace existence of NO_2^-. Meanwhile, the same control tests were conducted by feeding Ar under OCP and a current density of 50 mA cm^{-2} (Figures S12A and S12B). The results show the same phenomenon as in the N_2 case except that the much lower content of NO_2^- could be detected, which is in good agreement with the results as measured by the Nessler method (Table S5). Those results exclude the NO_2^- contamination from N_2 source. Besides, considering that ammonia

Table 2. Chromogenic reaction equations in detecting NO_2

Disproportionation and Azide reaction:
$2NO_2 + 2KOH \rightarrow KNO_3 + KNO_2 + H_2O$
$HCl + NO_2^- + H_2N\text{-}Ph\text{-}SO_3H \rightarrow ClN_2\text{-}Ph\text{-}SO_3^- + 2H_2O$
$ClN_2\text{-}Ph\text{-}SO_3^- + H_2N\text{-}Np \rightarrow H_2N\text{-}Np\text{-}N{=}N\text{-}Ph\text{-}SO_3^-$(magenta) $+HCl$
KI test paper reaction:
$NO_2 + KI \rightarrow 2KNO_3 + 2NO + I_2$ (blue)

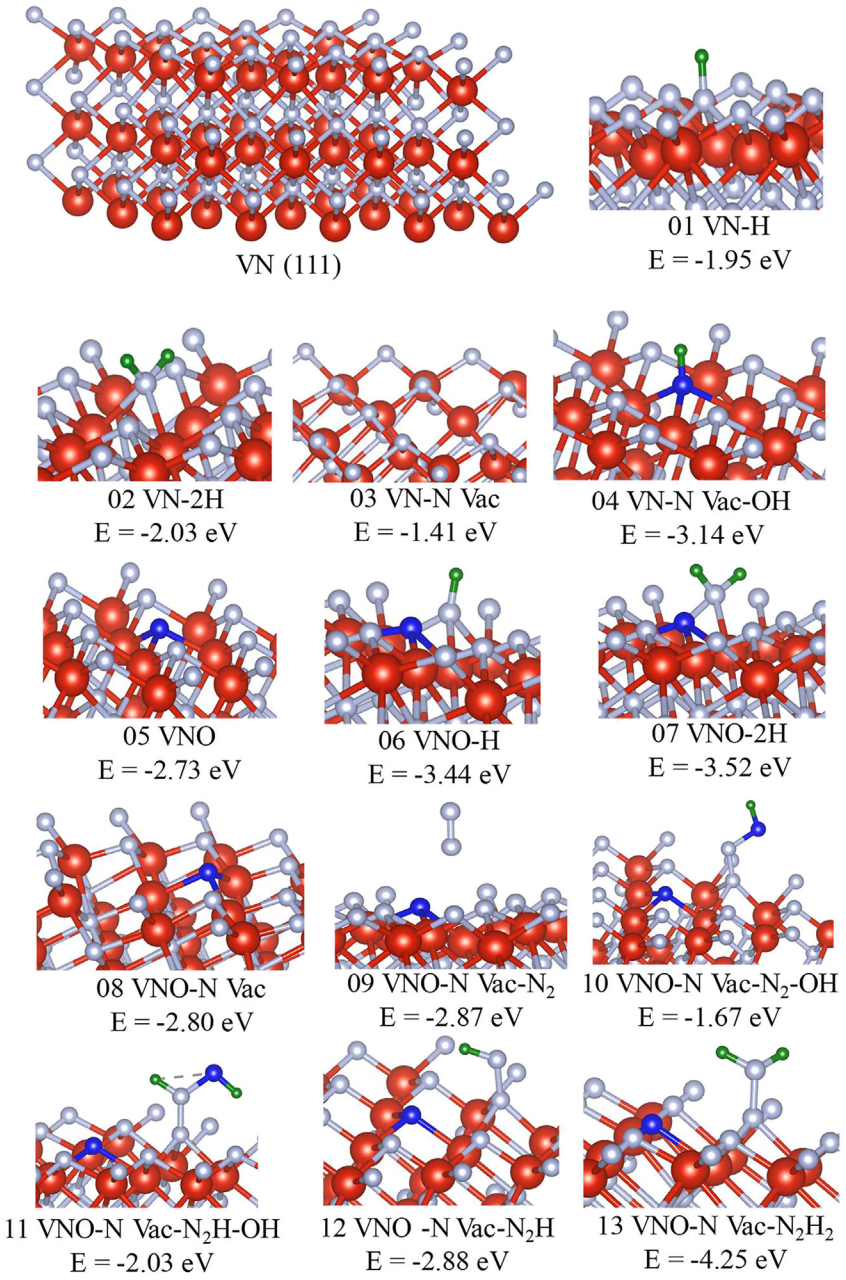

Figure 9. DFT calculations optimized geometric structures and intermediates on the VN NPs (Red: V, Gray: N, Blue: O, Green: H)

was generally derived from the electron-accepting process of nitrogen, the reduction reaction of $*NO_x$ must have happened.

With the membraneless configuration of the flow electrolyzer, the hydrogen produced from the HER at the cathode could transfer across the thinner electrolyte to the anode surface and reduce the *in-situ*-formed $*NO_x$ to produce ammonia conveniently. Figure 8C shows that the ammonia yield rate in the membraneless flow cell was approximately two times higher than that in the membrane flow cell. In addition, in the membraneless flow cell, hydrogen was detected on the anode side by GC measurement (Figure S6). The lower ammonia yield rate in the membrane flow cell could be ascribed to the blocked hydrogen permeation by the Nafion 211 membrane[53] and the trace ammonia contamination.[39]

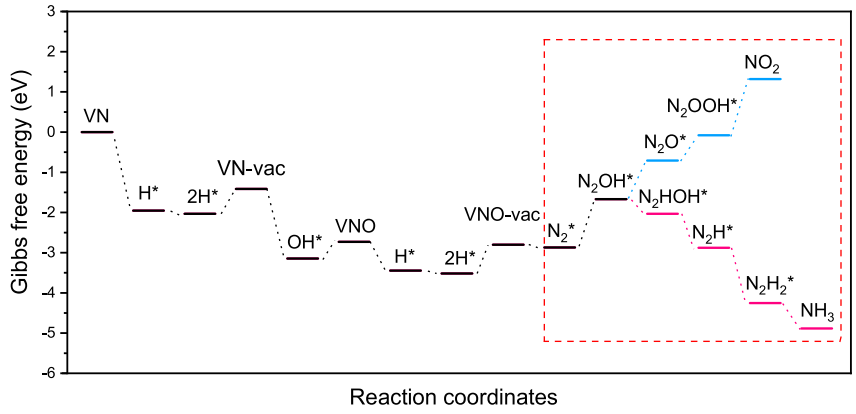

Figure 10. DFT calculations free energy evolution for ammonia and nitrogen dioxide formation on VN (111) at 0 V (vs RHE)

Furthermore, to verify the H_2-permeation reaction process in the membraneless cell, extra hydrogen was fed from the cathode side of the membrane flow cell, and the ammonia yield rate obviously increased (Figure 8C). Conversely, when replacing the cathode with IrO_2 NPs-loaded GDL or bare GDL (Table S6), which are generally recognized to have low activity toward HER, ammonia formation would be suppressed. These results evidently proved the ammonia formation process should be the coupling of the NOR and HER.

The yellow V_2O_5 NPs (Figure S13A Inset), which were directly converted from the commercial VN NPs by pyrolysis treatment in air, showed almost no ENH activity (Figure S13 and Table S7). In conjunction with the isotopic labeling results (Figure 4E), a similar mechanism to the Mars-van Krevelen mechanism in NRR can be proceeded in ENH,[9,10,54] in which N_2 exchanges with N from VN to form ammonia. DFT calculations were carried out to further verify the coupling mechanism of NOR and HER (see STAR Methods for details) and the higher selectivity of ammonia than nitrogen oxide on VN (111). As depicted in Figures 9 and 10, the VN catalyst was firstly activated through energetically favorable hydrogenation and oxidation processes to form oxygen-doped VN with nitrogen vacancy (VNO-vac) sites. Meanwhile, some nitrogen on the catalyst surface was lost as a nitrogen source to form ammonia, and vacancies for adsorbing N_2 were left. This mechanism explained the nitrogen exchange between the catalyst and N_2, in good accordance

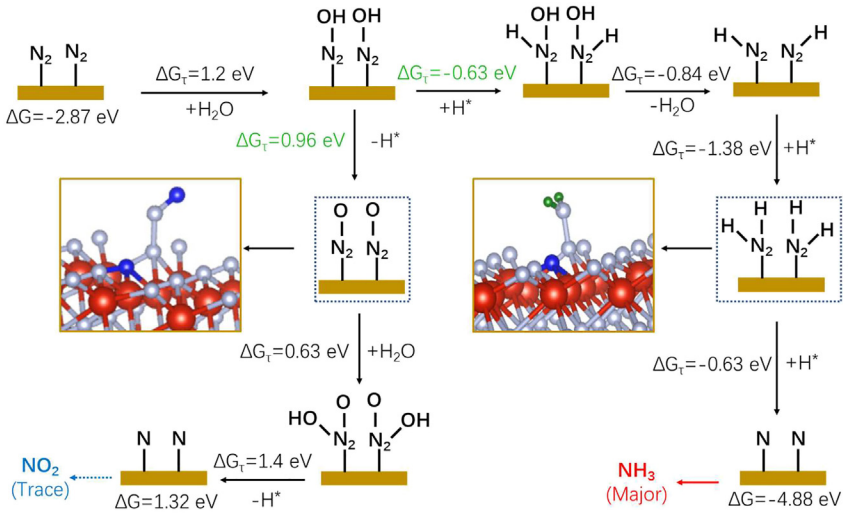

Figure 11. DFT calculations proposed mechanism for ammonia and nitrogen dioxide formation on VNO-vac sites

with the isotopic results for both $^{15}NH_4^+$ and $^{14}NH_4^+$ (Figure 4E) and the previously reported electrochemical NRR on VN NPs.[9]

Theoretically, VNO-vac sites would subsequently adsorb N_2 molecules (N_2*) and then preferentially convert them into hydrogenated nitrogen oxides (N_2OH*) at oxidation potentials (Figure 11). Under an atmosphere with H_2, the N_2OH* intermediate preferentially forms N_2HOH* through a chemical hydrogenation pathway ($\Delta G_\tau = -0.63$ eV) in competition with N_2O* from dehydration proton-coupled electron transfer ($\Delta G_\tau = 0.96$ eV). The following steps in the ammonia formation process are all more energetically favorable than those of nitrogen oxides (NO_2, Figure 10). The ultra-low concentration of NO_2 could be removed by the flowing electrolyte or *in-situ* converted to ammonia by H_2. Therefore, ammonia is the major product even at the oxidation potential following the pathway of N_2—N_2OH— N_2OH_2—N_2H—N_2H_2—NH_3, in well accordance with the experimental observations (Figures 4 and 8). In addition, due to the lower kinetics of the HER in alkaline media than in acidic media,[55] ammonia formation was impeded in the first 400 s at a current density of 50 mA cm^{-2} (Figure S13). Once sufficient H_2 was produced in the system (Figure S14 and S15), the ammonia yield returned to normal and was almost the same as that in acidic media (Figures 6A and S14C). These results strongly demonstrated the efficient production of ammonia through the coupling of NOR and water splitting in one single flow electrolyzer.

DISCUSSION

In summary, a nitrogen fixation strategy for electrochemical ammonia synthesis from nitrogen and water was proposed. This method has the benefit of high yield under ambient conditions through the coherent cooperation of anodic nitrogen oxidation and cathodic hydrogen evolution. Systematic investigations and experimental results demonstrate that the coupled anodic NOR and cathodic HER accelerated the ammonia synthesis from N_2 in a membraneless flow electrolyzer. The process promoted ammonia production (ammonia yield rate: 9.9 mmol g^{-1} h^{-1} (0.029 mmol cm^{-2} h^{-1}), Faradaic efficiency: 4.8%), and alleviated circumambient ammonia contamination. Moreover, simulation model further revealed the reaction mechanism and indicated that the coupled NOR and HER process could improve energy efficiency and facilitate the overall ammonia synthesis process. We believe this electrochemical integration strategy positively promotes the ammonia production yield and detection accuracy toward ammonia synthesis from nitrogen and water. Future studies may find or design suitable gas diffusion layers and the rational cell creation for promoting the development of nitrogen fixation through the electrochemical pathway.

Limitations of the study

The very limited N_2 solubility in aqueous media severely drags down the efficiency for electrochemical fixation of nitrogen. Meanwhile, most of the NRR/NOR performance associating electrochemical current density is far from enough to industrially obtain profits. To overcome those bottleneck problems, it is highly urgent to design advanced cell configuration with well-defined gas-liquid-solid triple-phase interface in the absence of mass transport limitations. Hence, vast efforts should also be devoted to the novel cell design for promoting the development of nitrogen fixation through electrochemical pathway in the prospective study.

STAR★METHODS

Detailed methods are provided in the online version of this paper and include the following:

- KEY RESOURCES TABLE
- RESOURCE AVAILABILITY
  - Lead contact
  - Materials availability
  - Data and code availability
- METHOD DETAILS
  - Material characterization
  - Flow cell electrolysis
  - Product quantification
  - $^{15}N_2$ electrolysis
  - Computational methods

SUPPLEMENTAL INFORMATION

Supplemental information can be found online at https://doi.org/10.1016/j.isci.2023.106407.

ACKNOWLEDGMENTS

This work was sponsored by the National Natural Science Foundation of China (22074062, 52072273, 52201227), the State Key Laboratory of Pollution Control and Resource Reuse (PCRR-ZZ-202106), the Fundamental Research Funds for the Central Universities (021114380183, 021114380189, 021114380199), the Research Funds from Frontiers Science Center for Critical Earth Material Cycling of Nanjing University, and Research Funds for Jiangsu Distinguished Professor.

AUTHOR CONTRIBUTIONS

J.-J.L.: Methodology, Investigation, Visualization, Writing – original draft. Z.L.: Formal analysis, Resources. J.F.: Methodology, Writing – review & editing. W.Z.: Methodology, Conceptualization, Supervision, Writing – original draft.

DECLARATION OF INTERESTS

The authors declare no conflict of interest.

Received: October 12, 2022
Revised: February 21, 2023
Accepted: March 10, 2023
Published: March 21, 2023

REFERENCES

1. Chen, J.G., Crooks, R.M., Seefeldt, L.C., Bren, K.L., Bullock, R.M., Darensbourg, M.Y., Holland, P.L., Hoffman, B., Janik, M.J., Jones, A.K., et al. (2018). Beyond fossil fuel–driven nitrogen transformations. Science *360*, eaar6611.

2. Burén, S., and Rubio, L.M. (2018). State of the art in eukaryotic nitrogenase engineering. FEMS Microbiol. Lett. *365*. fnx274–9. https://doi.org/10.1093/femsle/fnx274.

3. Lee, C.C., Ribbe, M.W., and Hu, Y. (2014). Cleaving the N,N triple bond: the transformation of dinitrogen to ammonia by nitrogenases. Met. Ions Life Sci. *14*, 147–176. https://doi.org/10.1007/978-94-017-9269-1_7.

4. Cui, X., Tang, C., and Zhang, Q. (2018). A review of electrocatalytic reduction of dinitrogen to ammonia under ambient conditions. Adv. Energy Mater. *8*, 1800369. https://doi.org/10.1002/aenm.201800369.

5. Yan, Z., Ji, M., Xia, J., and Zhu, H. (2020). Recent advanced materials for electrochemical and photoelectrochemical synthesis of ammonia from dinitrogen: one step closer to a sustainable energy future. Adv. Energy Mater. *10*, 1902020. https://doi.org/10.1002/aenm.201902020.

6. Foster, S.L., Bakovic, S.I.P., Duda, R.D., Maheshwari, S., Milton, R.D., Minteer, S.D., Janik, M.J., Renner, J.N., and Greenlee, L.F. (2018). Catalysts for nitrogen reduction to ammonia. Nat. Catal. *1*, 490–500. https://doi.org/10.1038/s41929-018-0092-7.

7. Soloveichik, G. (2019). Electrochemical synthesis of ammonia as a potential alternative to the Haber–Bosch process. Nat. Catal. *2*, 377–380. https://doi.org/10.1038/s41929-019-0280-0.

8. Lazouski, N., Chung, M., Williams, K., Gala, M.L., and Manthiram, K. (2020). Non-aqueous gas diffusion electrodes for rapid ammonia synthesis from nitrogen and water-splitting-derived hydrogen. Nat. Catal. *3*, 463–469. https://doi.org/10.1038/s41929-020-0455-8.

9. Yang, X., Nash, J., Anibal, J., Dunwell, M., Kattel, S., Stavitski, E., Attenkofer, K., Chen, J.G., Yan, Y., and Xu, B. (2018). Mechanistic insights into electrochemical nitrogen reduction reaction on vanadium nitride nanoparticles. J. Am. Chem. Soc. *140*, 13387–13391. https://doi.org/10.1021/jacs.8b08379.

10. Yang, X., Kattel, S., Nash, J., Chang, X., Lee, J.H., Yan, Y., Chen, J.G., and Xu, B. (2019). Quantification of active sites and elucidation of reaction mechanism of electrochemical nitrogen reduction reaction on vanadium nitride. Angew. Chem., Int. Ed. Engl. *58*, 13768–13772. https://doi.org/10.1002/anie.201906449.

11. Ren, Y., Yu, C., Tan, X., Huang, H., Wei, Q., and Qiu, J. (2021). Strategies to suppress hydrogen evolution for highly selective electrocatalytic nitrogen reduction: challenges and perspectives. Energy Environ. Sci. *14*, 1176–1193. https://doi.org/10.1039/D0EE03596C.

12. Rosca, V., Duca, M., de Groot, M.T., and Koper, M.T.M. (2009). Nitrogen cycle electrocatalysis. Chem. Rev. *109*, 2209–2244. https://doi.org/10.1021/cr8003696.

13. Hao, Y.-C., Guo, Y., Chen, L.-W., Shu, M., Wang, X.-Y., Bu, T.-A., Gao, W.-Y., Zhang, N., Su, X., Feng, X., et al. (2019). Promoting nitrogen electroreduction to ammonia with bismuth nanocrystals and potassium cations in water. Nat. Catal. *2*, 448–456. https://doi.org/10.1038/s41929-019-0241-7.

14. Wang, M., Liu, S., Qian, T., Liu, J., Zhou, J., Ji, H., Xiong, J., Zhong, J., and Yan, C. (2019). Over 56.55% Faradaic efficiency of ambient ammonia synthesis enabled by positively shifting the reaction potential. Nat. Commun. *10*, 341. https://doi.org/10.1038/s41467-018-08120-x.

15. Yu, X., Han, P., Wei, Z., Huang, L., Gu, Z., Peng, S., Ma, J., and Zheng, G. (2018). Boron-doped graphene for electrocatalytic N_2 reduction. Joule *2*, 1610–1622. https://doi.org/10.1016/j.joule.2018.06.007.

16. Zhou, F., Azofra, L.M., Ali, M., Kar, M., Simonov, A.N., McDonnell-Worth, C., Sun, C., Zhang, X., and MacFarlane, D.R. (2017). Electro-synthesis of ammonia from nitrogen at ambient temperature and pressure in ionic liquids. Energy Environ. Sci. *10*, 2516–2520. https://doi.org/10.1039/C7EE02716H.

17. Chen, G.-F., Cao, X., Wu, S., Zeng, X., Ding, L.-X., Zhu, M., and Wang, H. (2017). Ammonia electrosynthesis with high selectivity under ambient conditions via a Li^+ incorporation strategy. J. Am. Chem. Soc. *139*, 9771–9774. https://doi.org/10.1021/jacs.7b04393.

18. Yao, Y., Zhu, S., Wang, H., Li, H., and Shao, M. (2018). A spectroscopic study on the nitrogen electrochemical reduction reaction on gold

and platinum surfaces. J. Am. Chem. Soc. *140*, 1496–1501. https://doi.org/10.1021/jacs.7b12101.

19. Du, H.-L., Chatti, M., Hodgetts, R.Y., Cherepanov, P.V., Nguyen, C.K., Matuszek, K., MacFarlane, D.R., and Simonov, A.N. (2022). Electroreduction of nitrogen at almost 100% current-to-ammonia efficiency. Nature *609*, 722–727. https://doi.org/10.1038/s41586-022-05108-y.

20. Zhang, X., Cao, Y., Huang, Z., Zhang, S., Liu, C., Pan, L., Shi, C., Zhang, X., Zhou, Y., Yang, G., and Zou, J. (2022). Regulating the interfacial charge transfer and constructing symmetry-breaking sites for the enhanced N_2 electroreduction activity. Carbon Energy, 5–8. https://doi.org/10.1002/cey2.266.

21. Wu, T., Liu, Q., Xing, Z., Mou, S., Li, C., Qiao, Y., Zhu, X., Luo, Y., Shi, X., Zhang, Y., and Sun, X. (2019). Greatly improving electrochemical N_2 reduction over TiO_2 nanoparticle by Fe doping. Angew. Chem., Int. Ed. Engl. *58*, 18449–18453. https://doi.org/10.1002/anie.201911153.

22. Andersen, S.Z., Čolić, V., Yang, S., Schwalbe, J.A., Nielander, A.C., McEnaney, J.M., Enemark-Rasmussen, K., Baker, J.G., Singh, A.R., Rohr, B.A., et al. (2019). A rigorous electrochemical ammonia synthesis protocol with quantitative isotope measurements. Nature *570*, 504–508. https://doi.org/10.1038/s41586-019-1260-x.

23. Chen, G., Ren, S., Zhang, L., Cheng, H., Luo, Y., Zhu, K., Ding, L., and Wang, H. (2019). Advances in electrocatalytic N_2 reduction—strategies to Tackle the selectivity challenge. Small Methods *3*, 1800337. https://doi.org/10.1002/smtd.201800337.

24. Chen, Y., Liu, H., Ha, N., Licht, S., Gu, S., and Li, W. (2020). Revealing nitrogen-containing species in commercial catalysts used for ammonia electrosynthesis. Nat. Catal. *3*, 1055–1061. https://doi.org/10.1038/s41929-020-00527-4.

25. Suryanto, B.H.R., Du, H.-L., Wang, D., Chen, J., Simonov, A.N., and MacFarlane, D.R. (2019). Challenges and prospects in the catalysis of electroreduction of nitrogen to ammonia. Nat. Catal. *2*, 290–296. https://doi.org/10.1038/s41929-019-0252-4.

26. Fowler, D., Coyle, M., Skiba, U., Sutton, M.A., Cape, J.N., Reis, S., Sheppard, L.J., Jenkins, A., Grizzetti, B., Galloway, J.N., et al. (2013). The global nitrogen cycle in the twenty-first century. Philos. Trans. R. Soc. Lond. B. Biol. Sci. *368*, 20130164.

27. Patil, B.S., Wang, Q., Hessel, V., and Lang, J. (2015). Plasma N_2-fixation: 1900–2014. Catal. Today *256*, 49–66.

28. Dai, C., Sun, Y., Chen, G., Fisher, A.C., and Xu, Z.J. (2020). Electrochemical oxidation of nitrogen towards direct nitrate production on spinel oxides. Angew. Chem., Int. Ed. Engl. *59*, 9418–9422. https://doi.org/10.1002/anie.202002923.

29. Kuang, M., Wang, Y., Fang, W., Tan, H., Chen, M., Yao, J., Liu, C., Xu, J., Zhou, K., and Yan, Q. (2020). Efficient nitrate synthesis via ambient nitrogen oxidation with Ru-doped TiO_2/RuO_2 electrocatalysts. Adv. Mater. *32*, 2002189. https://doi.org/10.1002/adma.202002189.

30. Guo, S., Heck, K., Kasiraju, S., Qian, H., Zhao, Z., Grabow, L.C., Miller, J.T., and Wong, M.S. (2018). Insights into nitrate reduction over indium-decorated palladium nanoparticle catalysts. ACS Catal. *8*, 503–515. https://doi.org/10.1021/acscatal.7b01371.

31. Clark, C.A., Reddy, C.P., Xu, H., Heck, K.N., Luo, G., Senftle, T.P., and Wong, M.S. (2020). Mechanistic insights into pH-controlled nitrite reduction to ammonia and hydrazine over rhodium. ACS Catal. *10*, 494–509. https://doi.org/10.1021/acscatal.9b03239.

32. Elias, W.C., Heck, K.N., Guo, S., Yazdi, S., Ayala-Orozco, C., Grossweiler, S., Domingos, J.B., Ringe, E., and Wong, M.S. (2020). Indium-decorated Pd nanocubes degrade nitrate anions rapidly. Appl. Catal. B Environ. *276*, 119048.

33. Jung, S., Bae, S., and Lee, W. (2014). Development of Pd–Cu/hematite catalyst for selective nitrate reduction. Environ. Sci. Technol. *48*, 9651–9658. https://doi.org/10.1021/es502263p.

34. Lv, J.-J., Jouny, M., Luc, W., Zhu, W., Zhu, J.-J., and Jiao, F. (2018). A highly porous copper electrocatalyst for carbon dioxide reduction. Adv. Mater. *30*, 1803111–1803119. https://doi.org/10.1002/adma.201803111.

35. Luc, W., Fu, X., Shi, J., Lv, J.-J., Jouny, M., Ko, B.H., Xu, Y., Tu, Q., Hu, X., Wu, J., et al. (2019). Two-dimensional copper nanosheets for electrochemical reduction of carbon monoxide to acetate. Nat. Catal. *2*, 423–430. https://doi.org/10.1038/s41929-019-0269-8.

36. Du, H., Fu, J., Liu, L.-X., Ding, S., Lyu, Z., Chang, Y.-C., Jin, X., Kengara, F.O., Song, B., Min, Q., et al. (2022). Recent progress in electrochemical reduction of carbon monoxide toward multi-carbon products. Mater. Today *59*, 182–199.

37. Liu, J., Cai, Y., Song, R., Ding, S., Lyu, Z., Chang, Y.-C., Tian, H., Zhang, X., Du, D., Zhu, W., et al. (2021). Recent progress on single-atom catalysts for CO_2 electroreduction. Mater. Today *48*, 95–114.

38. Lv, J.-J., Yin, R., Zhou, L., Li, J., Kikas, R., Xu, T., Wang, Z.-J., Jin, H., Wang, X., and Wang, S. (2022). Microenvironment engineering for the electrocatalytic CO_2 reduction reaction. Angew. Chem., Int. Ed. Engl. *61*, e202207252. https://doi.org/10.1002/anie.202207252.

39. Ren, Y., Yu, C., Tan, X., Han, X., Huang, H., Huang, H., and Qiu, J. (2019). Is it appropriate to use the nafion membrane in electrocatalytic N_2 reduction? Small Methods *3*, 1900474. https://doi.org/10.1002/smtd.201900474.

40. Tang, C., and Qiao, S.-Z. (2019). True or false in electrochemical nitrogen reduction. Joule *3*, 1573–1575.

41. Du, H.-L., Gengenbach, T.R., Hodgetts, R., MacFarlane, D.R., and Simonov, A.N. (2019). Critical assessment of the electrocatalytic activity of vanadium and niobium nitrides toward dinitrogen reduction to ammonia. ACS Sustain. Chem. Eng. *7*, 6839–6850. https://doi.org/10.1021/acssuschemeng.8b06163.

42. Lv, X.-W., Liu, Y., Wang, Y.-S., Liu, X.-L., and Yuan, Z.-Y. (2021). Encapsulating vanadium nitride nanodots into N,S-codoped graphitized carbon for synergistic electrocatalytic nitrogen reduction and aqueous Zn-N_2 battery. Appl. Catal. B Environ. *280*, 119434.

43. Shi, L.-N., Li, X.-Z., Cui, L.-T., Wang, P.-F., Xie, Y., and Yi, T.-F. (2022). Recent progresses and perspectives of VN-based materials in the application of electrochemical energy storage. J. Ind. Eng. Chem. *114*, 52–76.

44. Luc, W., Ko, B.H., Kattel, S., Li, S., Su, D., Chen, J.G., and Jiao, F. (2019). SO_2-Induced selectivity change in CO_2 electroreduction. J. Am. Chem. Soc. *141*, 9902–9909. https://doi.org/10.1021/jacs.9b03215.

45. Möller, S., Barwe, S., Masa, J., Wintrich, D., Seisel, S., Baltruschat, H., and Schuhmann, W. (2020). Online monitoring of electrochemical carbon corrosion in alkaline electrolytes by differential electrochemical mass spectrometry. Angew. Chem., Int. Ed. Engl. *59*, 1585–1589. https://doi.org/10.1002/anie.201909475.

46. Lin, Y.-X., Zhang, S.-N., Xue, Z.-H., Zhang, J.-J., Su, H., Zhao, T.-J., Zhai, G.-Y., Li, X.-H., Antonietti, M., and Chen, J.-S. (2019). Boosting selective nitrogen reduction to ammonia on electron-deficient copper nanoparticles. Nat. Commun. *10*, 4380. https://doi.org/10.1038/s41467-019-12312-4.

47. Shi, M.-M., Bao, D., Wulan, B.-R., Li, Y.-H., Zhang, Y.-F., Yan, J.-M., and Jiang, Q. (2017). Au sub-nanoclusters on TiO_2 toward highly efficient and selective electrocatalyst for N_2 conversion to NH_3 at ambient conditions. Adv. Mater. *29*, 1606550. https://doi.org/10.1002/adma.201606550.

48. He, C., Wu, Z.-Y., Zhao, L., Ming, M., Zhang, Y., Yi, Y., and Hu, J.-S. (2019). Identification of FeN4 as an efficient active site for electrochemical N_2 reduction. ACS Catal. *9*, 7311–7317. https://doi.org/10.1021/acscatal.9b00959.

49. Cao, W., Wang, Z., Zeng, Q., and Shen, C. (2016). ^{13}C NMR and XPS characterization of anion adsorbent with quaternary ammonium groups prepared from rice straw, corn stalk and sugarcane bagasse. Appl. Surf. Sci. *389*, 404–410.

50. Chen, P., Wang, L.-K., Wang, G., Gao, M.-R., Ge, J., Yuan, W.-J., Shen, Y.-H., Xie, A.-J., and Yu, S.-H. (2014). Nitrogen-doped nanoporous carbon nanosheets derived from plant biomass: an efficient catalyst for oxygen reduction reaction. Energy Environ. Sci. *7*, 4095–4103. https://doi.org/10.1039/C4EE02531H.

51. Miranda, K.M., Espey, M.G., and Wink, D.A. (2001). A rapid, simple spectrophotometric

method for simultaneous detection of nitrate and nitrite. Nitric Oxide *5*, 62–71.

52. O'Neill, E., and Hinrichs, R.Z. (2011). Production of molecular iodine from the heterogeneous reaction of nitrogen dioxide with solid potassium iodide. J. Geophys. Res. *116*, D01301. https://doi.org/10.1029/2010JD014880.

53. Ye, D., Tu, Z., Yu, Y., Cai, Y., Zhang, H., Zhan, Z., and Pan, M. (2014). Hydrogen permeation across super-thin membrane and the burning limitation in low-temperature proton exchange membrane fuel cell. Int. J. Energy Res. *38*, 1181–1191. https://doi.org/10.1002/er.3136.

54. Abghoui, Y., and Skúlason, E. (2017). Electrochemical synthesis of ammonia via Mars-van Krevelen mechanism on the (111) facets of group III–VII transition metal mononitrides. Catal. Today *286*, 78–84.

55. Jouny, M., Luc, W., and Jiao, F. (2018). High-rate electroreduction of carbon monoxide to multi-carbon products. Nat. Catal. *1*, 748–755. https://doi.org/10.1038/s41929-018-0133-2.

56. Perdew, J.P., Burke, K., and Ernzerhof, M. (1996). Generalized gradient approximation made simple. Phys. Rev. Lett. *77*, 3865–3868. https://doi.org/10.1103/PhysRevLett.77.3865.

57. Kresse, G., and Joubert, D. (1999). From ultrasoft pseudopotentials to the projector augmented-wave method. Phys. Rev. B *59*, 1758–1775. https://doi.org/10.1103/PhysRevB.59.1758.

58. Monkhorst, H.J., and Pack, J.D. (1976). Special points for Brillouin-zone integrations. Phys. Rev. B *13*, 5188–5192. https://doi.org/10.1103/PhysRevB.13.5188.

59. Henkelman, G., and Jónsson, H. (2000). Improved tangent estimate in the nudged elastic band method for finding minimum energy paths and saddle points. J. Chem. Phys. *113*, 9978–9985. https://doi.org/10.1063/1.1323224.

STAR★METHODS

KEY RESOURCES TABLE

REAGENT or RESOURCE	SOURCE	IDENTIFIER
Chemicals, peptides, and recombinant proteins		
VN NPs	3A Chemicals Co., Ltd	CAS: 24646-85-3
Bulk VN	3A Chemicals Co., Ltd	CAS: 24646-85-3
Pt/C (20 wt% Pt)	Johnson Matthey	CAS: 7740-06-4
NH4Cl	Aladdin	CAS: 12125-02-9
H2SO4	Fisher	CAS: 7664-93-9
KOH	Aladdin	CAS: 1310-58-3
Dimethyl sulfoxide	Alfa Aesar	CAS: 67-68-5
D2O	Energy Chemical	CAS:7789-20-0
HANNA agent	HANNA Inc.	Product number: HI93715-05
p-aminobenzene-sulfonamide	Adamas-beta	CAS: 63-74-1
N-(1-Naphthyl) ethylenediamine dihydrochloride	Aladdin	CAS: 1465-25-4
KI test paper	Shanghai SSS Reagent Co., Ltd	Product number: C148-2017
N_2 (99.999%)	Nanjing Tianze Gas Co., Ltd	CAS: 7727-37-9
N_2 (^{15}N, 98%)	Sigma-Aldrich	CAS: 29817-79-6
Ar (99.999%)	Nanjing Tianze Gas Co., Ltd	CAS: 7740-37-1
Nafion (10 wt% aqueous solution)	Fuel Cell Store	CAS: 66796-30-3
Gas diffusion layer	Fuel Cell Store	Product number: Sigracet 29 BC
Nafion 211 membrane	Fuel Cell Store	Product number: 1600001-2
Software and algorithms		
Graph plotting	Origin Lab	Origin: Data Analysis and Graphing Software (originlab.com)
VASP 5.3.5	VASP Software	VASP - Vienna Ab initio Simulation Package
Other		
SEM	LEO153VP, ZEISS Inc.	https://www.zeiss.com.cn/microscopy/products/electron-microscopy/evo.html
TEM	JEM-2800, JEOL Inc.	http://www.bahens.cn/product/55.html
XRD	D8 ADVANCE, Bruker Inc.	https://www.instrument.com.cn/netshow/C123139.htm
XPS	PHI 5000, HITACHI Inc.	https://www.instrument.com.cn/netshow/C191769.htm
Ammonia detector	HI96715, HANNA Inc.	https://b2b.baidu.com/land?id=bb23248c6763b817cd5391f1e80eafdd10
UV spectrophotometer	UH5300, ULVAC-PHI, Inc.	http://www.app17.com/c143174/products/d9951153.html

RESOURCE AVAILABILITY

Lead contact

Further information and requests for resources and reagents should be directed to and will be fulfilled by the lead contact, Wenlei Zhu (wenleizhu@nju.edu.cn).

Materials availability

This study did not generate new unique reagents.

Data and code availability

- Original data reported in this paper will be shared by the lead contact upon request.
- This paper does not report original code.

- Any additional information required to reanalyze the data reported in this paper is available from the lead contact upon request.

METHOD DETAILS

Material characterization

All chemicals were of analytical grade without further purification unless otherwise noted. Commercial vanadium nitride nanoparticles with 40 nm diameter (VN NPs) and bulk vanadium nitride nanoparticles with 500 nm diameter (bulk VN) were used as catalysts in this work and bought from 3A Chemicals Co., Ltd. (Shanghai, China). The microstructure of the catalysts was characterized by field emission scanning electron microscopy (SEM, LEO153VP, 10 kV) with an energy-dispersive X−ray (EDS) spectrometer and high-resolution transmission electron microscopy (HRTEM, JEOL, JEM-2800). Powder X-ray diffraction (PXRD) measurements were conducted on a D8 ADVANCE X-ray diffractometer (Bruker Corporation, America). X-ray photoelectron spectra (XPS) were measured on a PHI 5000 VersaProbe (Ulvac-Phi, Japan), and XPS fitting was conducted by CasaXPS software with the adventitious carbon peak calibrated to 284.8 eV. All peaks were fitted using a Gaussian/Lorentzian product line shape and a Shirley background. Ultraviolet-visible (UV) spectra were recorded on a UH5300 spectrophotometer (Shimadzu, Kyoto, Japan).

Flow cell electrolysis

Electrochemical measurements were performed on an Autolab potentiostat (PGSTAT 204) in a three-electrode system. In this study, the carbon paper with a microporous layer (Sigracet 29 BC, Fuel Cell Store, America) was used as the gas diffusion layer (GDL) for supporting catalysts, collecting current and acting as a pathway for gas from flow channels to the catalyst surface. A Pt/C (platinum, nominally 20% on carbon black, Alfa Aesar)-coated GDL with a loading of 0.5 mg cm^{-2} was used as the counter electrode unless otherwise noted. A saturated calomel electrode (SCE, saturated KCl, INESA Scientific Instrument CO., LTD) or Ag/AgCl (saturated KCl, CH Instruments, Inc.) electrode was used as the reference electrode (RE). A VN NPs-coated GDL was applied as the working electrode unless otherwise noted and was prepared by drop-casting a catalyst ink. We weighed the GDL before and after deposition to record its actual catalyst loading and maintained a loading of 3 mg cm^{-2} for all electrodes unless otherwise noted. To prepare the catalyst ink, 100 mg of catalyst was ultrasonically dispersed in a mixture of 3 mL of n-propanol and 20 μL of Nafion (10 wt% aqueous solution, Fuel Cell Store, America). Then, the mixture was sonicated for 30 min prior to dropcasting. Nafion 211 membrane (Fuel Cell Store) was used in the membrane flow cell.

The electrolysis experiments were performed in a two-channel flow cell (channels dimension 2 × 0.5 × 0.2 cm^3, Figure 2). The device was fabricated from acrylic and included a gas channel for feeding high-purity N_2 (99.999%), a liquid channel for flowing electrolytes, and solid acrylic end pieces. PTFE gaskets were placed between each component for sealing, and the device was tightened using six bolts. The electrode geometric area was 1 cm^2, and the distance between the anode and cathode was 2 mm. An external SCE (electrolyte of acidic media) or Ag/AgCl (electrolyte of alkaline media) reference electrode located ~5 cm from the inlet of the cathode was used to measure the anodic half-cell potential. All potential measurements were converted to the RHE based on the following formula: $E_{RHE} = E_{Hg/HgCl2} + E^{\theta}_{Hg/HgCl2} + 0.059 \times pH$ (in volts) or $E_{RHE} = E_{Ag/AgCl} + E^{\theta}_{Ag/AgCl} + 0.059 \times pH$ (in volts). The measured pH values of the bulk electrolyte were used for RHE conversions unless stated otherwise.

The N_2 (99.999%), Ar (99.999%), or air (pumped from the atmosphere) flow rate was set at 10 mL min^{-1} via a mass flow controller (Sevenstar, CS300). The flow rates of electrolyte, sulfuric acid (H_2SO_4 with different concentrations, 98%) or potassium hydroxide (1 M KOH, 99.99%) aqueous solution were controlled via a peristaltic pump (Chuangrui Precision Pump Co., Ltd., China), with the electrolyte flow rate set to 1 mL min^{-1} unless otherwise noted. Prior to electrochemical reactivity studies, all the electrodes assembled into the flow electrolyzer were first rinsed with the electrolyte at 1 mL min^{-1} for 15 min to clear surface impurities.

In the stability investigation experiments, a constant current density of 50 mA cm^{-2} was applied for 500 seconds in the membraneless flow cell with a VN NPs-coated GDL as the anode and Pt/C-coated GDL as the cathode. N_2 was fed into the cell at a flow rate of 10 mL min^{-1}. The same configuration was run for five cycles, and the cell was rinsed with fresh 0.05 M H_2SO_4 for 5 min with a flow rate of 1 mL min^{-1} after each cycle. To acquire the energy efficiency, the ENH test was performed at 50 mA cm^{-2} for ca. 20 minutes in a

membraneless flow cell with two electrodes, i.e., an anode (VN NPs on a GDL with a loading of 3 mg cm^{-2}) and cathode (Pt-C on a GDL with a loading of 0.5 mg cm^{-2}), in which the electrolyte was 0.05 M H_2SO_4 by feeding N_2 at a flow rate of 10 mL min^{-1}.

Product quantification

The amount of ammonia produced in one single-pass electrolysis was determined using the Nessler method without a condensing process. The calibration curves were made by using NH_4Cl solutions in 0.05 M H_2SO_4 (adjusting pH to 13.5 with 1 M KOH solution) or 1 M KOH solution with known concentrations using a photometer (HI 96715, HANNA). After ammonia in an acidic electrolyte was collected in an aseptic centrifuge tube, KOH solution (1 M) was added to adjust the pH of the solution to 13.5 before its qualification.

The quantification of the ammonia amount in single-pass electrolysis was also verified by using ^{1}H NMR (Bruker AVIII 500 MHz). The ^{1}H NMR spectra were obtained using a water suppression method with 1500 scans. Typically, 500 μL of collected single-pass electrolyte was mixed with 100 μL of internal standard solution [25 ppm (m/m) dimethyl sulfoxide (≥99.9%, Alfa Aesar) in D_2O (99.8%)]. Gas products from the anode were determined on a gas chromatograph (GC, Agilent 7890B) equipped with Hayesep D and Molsieve 5A columns leading to a thermal conductivity detector (TCD) and a Hayesep D column leading to a flame ionization detector (FID). Hydrogen and oxygen were measured using TCD, while monoxide was detected using FID.

The Faradaic efficiency (FE) of ammonia formation was calculated as follows:

$$FE(\%) = (3F \times C \times V)/Q \quad \text{Equation 1}$$

where F is the Faraday constant, C is the measured ammonia concentration, V is the volume of the electrolyte, and Q is the total charge passed through the electrode during electrolysis.

The yield rates of ammonia production were calculated by the following equations:

$$r_{(m,NH4+)} = (C \times V)/t \times m \quad \text{Equation 2}$$

$$r_{(A,NH4+)} = (C \times V)/t \times A \quad \text{Equation 3}$$

where C is the measured ammonia molar concentration, V is the volume of the electrolyte, t is the electrochemical oxidation reaction time, m is the loading mass of the electrocatalyst, and A is the geometric area of the working electrode.

The energy efficiency was calculated by the following equation:

$$\epsilon = \exists/n_{NH3} \quad \text{Equation 4}$$

where ∃ is the applied electric energy and n is the measured ammonia molar amount.

$^{15}N_2$ electrolysis

The labeled isotope experiment was performed using $^{15}N_2$ gas (98 at% $^{15}N_2$, Sigma-Aldrich) for electrolysis. Typically, $^{15}N_2$ was injected into the flow cell with a flow rate of 10 mL min^{-1}, and the flow rate of 0.05 M H_2SO_4 electrolyte was set at 1 mL min^{-1}. Electrolysis tests were conducted at a constant oxidation current of 50 mA cm^{-2} for two cycles with each cycle lasting 5 min, and the relevant single-pass electrolyte was collected for analysis by ^{1}H NMR.

Computational methods

All the calculations were performed with density functional theory (DFT) as implemented in the Vienna Ab initio Software Package (VASP 5.3.5) code, the Perdew–Burke–Ernzerhof (PBE) generalized gradient approximation and the projected augmented wave (PAW) method.[56,57] The cut-off energy for the plane-wave basis set was set to be 400 eV. The convergence criteria for the electronic self-consistent iteration and force were set to 10^{-5} eV and 0.01 eV/Å, respectively. A 4 × 4 supercell of the VN (111) surface including 6 atomic layers was constructed to model the catalyst in this work, with the bottom of two layers fixed in structural relaxation. The Brillouin zone of the surface unit cell was sampled by Monkhorst–Pack (MP) grids.[58] The VN (111) surface was determined by a 3 × 3 × 1 Monkhorst−Pack grid.[59] A vacuum layer of

15 Å was introduced to avoid interactions between periodic images. The adsorption energy (E_{ads}) of the surface species is defined by

$$E_{ads} = E_{total} - E_{surface} - E_{species} \quad \text{Equation 5}$$

where E_{total} represents the total energy of the adsorbed species on the catalyst surface, $E_{surface}$ is the energy of the empty surface, and $E_{species}$ is the energy of the species in the gas phase.